3D angle decomposition for elastic reverse time migration

Yuting Duan & Paul Sava
Center for Wave Phenomena, Colorado School of Mines

ABSTRACT
Common reflection-angle gathers are important tools for migration velocity analysis and amplitude-versus-angle (AVA) analysis. Angle gathers of acoustic (PP) and elastic (PS, SP, and SS) reflectivities provide information about different subsurface material properties. We propose 3D angle decomposition methods for elastic reverse time migration using time- and space-lag common image point gathers, time-lag common image gathers, and space-lag common image gathers computed from elastic wavefields. We compute time-lag common image gathers at multiple contiguous locations, instead of isolated positions as is commonly done with common image gathers. Then, we transform the extended images to the angle domain using slant stacks along surfaces that connect neighboring positions, instead of line slant stacks for isolated common image gathers. We demonstrate our methods using 2D and 3D synthetic examples and show that our techniques provide accurate opening and azimuth angles, and that they can handle steeply dipping reflectors and converted wave modes.

Key words: migration, angle gathers, elastic

1 INTRODUCTION

Common reflection-angle gathers are useful in migration velocity analysis and amplitude-versus-angle analysis. Angle decomposition techniques can be classified to two categories, depending on the type of migration used: ray-based methods and wavefield-based methods. Ray-based method (Brandsberg-Dahl et al., 1999; Audebert et al., 2000; Xu et al., 2001) are convenient, as it is straightforward and efficient to obtain angle information from ray-paths traced to an image point. However, the accuracy of ray-based algorithms suffers in areas where velocity contrasts are strong, for example, in presence of salt bodies. Wavefield-based angle-decomposition methods rely on decomposition of the wavefield in its plane wave components (De Bruin et al., 1990; Wu and Xie, 2002; Sava and Fomel, 2003; Biondi and Symes, 2004; Yoon et al., 2004; Sava, 2007; Xu et al., 2011; Sava and Vlad, 2011). Although more computationally expensive compared to ray-based method, the wavefield-based methods are superior because they accurately simulate wave propagation in complex geologic structures.

Wavefield-based methods generally fall into two categories: pre-migration and post-migration algorithms (Vyas et al., 2011). Pre-migration methods refer to methods that decompose the wavefields prior to the imaging condition, for example, $f-k$ domain decomposition (Xu et al., 2011), or Poynting vector methods (Yoon and Marfurt, 2006; Yan and Ross, 2013). The $f-k$ domain decomposition requires 4D Fourier transforms in 3D models, so the computational cost can be high. Poynting vector methods are less computationally intensive, but may yield inaccurate angle information when wavefields are complicated, for example, by triplicated wavefronts (Patrikeeva and Sava, 2013). Post-migration methods, which decompose migrated images to angle gathers after the imaging condition, require two steps: computation of extended images as a function of space- or time-lag gathers followed by mapping of the extended domain to the angle domain (Sava and Vasconcelos, 2009; Sava and Vlad, 2011). Sava and Fomel (2006) describe algorithms for angle decomposition using space-lag (λCIG), time-lag (τCIG), and mixed time- and space-lag common image point (CIP) gathers. Angle gathers computed using the λCIGs or τCIGs describe the reflectivity as a function of reflection angles and a space axis, typically the depth axis, while for CIPs, the angle-dependent reflectivity is evaluated at selected points in the subsurface. These methods can handle complicated wavefield with wavefront triplication.

Wavefield-based angle-decomposition methods can be extended to elastic and anisotropic media. Sava and Alkhalifah (2013) propose a technique for mapping CIP gathers to angle gathers in 3D TI media, with wavefields constructed by solving a pseudo-acoustic wave equation. Algorithms for elastic wavefield based angle decomposition have also been proposed (Yan and Sava, 2008; Yan and Xie, 2012). One important issue in angle decomposition using elastic wavefields is choice of imaging condition. A proper imaging condition is needed to separate different wave-modes. Yan and Sava (2008) propose an extended imaging condition that crosscorrelates decomposed P and S wavefields from the source and receiver. The amplitudes of computed CIGs for different types of re-

flections (PP, PS, SP, and SS) are related to their reflection coefficients, and these CIGs can be mapped to the angle domain through a process similar to that used in the acoustic case. However, PS or SP CIGs have three non-zero components in 3D, which are challenging to combine into one angle gather. Duan and Sava (2015) propose a scalar imaging condition for converted waves, which generates 3D PS and SP scalar images. This imaging condition makes it convenient to compute 3D angle gathers from the elastic wavefields.

This paper presents methods for opening and azimuth angle decomposition methods from elastic RTM. We develop the extended scalar imaging condition from the zero-lag scalar imaging condition. Our methods utilize local plane wave decompositions of extended images and exploits the relationships between the time-lag, space-lag, and image shift in space. Their relationships lead to opening and azimuth angle decomposition methods using either time-lag common image gather (τCIGs), space-lag common image gathers (λCIGs), or time- and space-lag common image point (CIP) gathers. To demonstrate the algorithms, we apply the angle decomposition to 3D elastic time- and space-lag and 2D elastic time-lag extended images.

2 ELASTIC SCALAR IMAGING CONDITION

Duan and Sava (2015) develop a scalar imaging condition using geometrical relationships between the propagation directions for the P and S wavefields, the reflector orientation, and the S-mode polarization direction. The PS and SP images computed using this imaging condition are scalars without polarity reversal. Combining the scalar imaging conditions for converted waves with the PP and SS imaging conditions proposed by Yan and Sava (2008), we obtain the elastic imaging condition:

$$I^{PP}(\mathbf{x}) = \sum_{e,t} P_s(e,\mathbf{x},t)\, P_r(e,\mathbf{x},t) \ , \tag{1}$$

$$I^{PS}(\mathbf{x}) = \sum_{e,t} \left[\nabla P_s(e,\mathbf{x},t) \times \mathbf{n}(\mathbf{x})\right] \cdot \mathbf{S}_r(e,\mathbf{x},t) \ , \tag{2}$$

$$I^{SP}(\mathbf{x}) = \sum_{e,t} \left[(\nabla \times \mathbf{S}_s(e,\mathbf{x},t)) \cdot \mathbf{n}(\mathbf{x})\right] P_r(e,\mathbf{x},t) \ , \tag{3}$$

$$I^{SS}(\mathbf{x}) = \sum_{e,t} \mathbf{S}_s(e,\mathbf{x},t) \cdot \mathbf{S}_r(e,\mathbf{x},t) \ . \tag{4}$$

Vector $\mathbf{n}(\mathbf{x})$ is the normal to the reflector plane. Quantities $P(e,\mathbf{x},t)$ and $\mathbf{S}(e,\mathbf{x},t)$ represent P and S wavefields obtained by wave-mode decomposition, as functions of experiment e, time t, and space $\mathbf{x}$. Subscripts s and r indicate the wavefield origins at source or receivers, respectively. The P and S wavefields are obtained from displacement wavefields using Helmholtz decomposition (Dellinger and Etgen, 1990; Yan and Sava, 2008):

$$P(e,\mathbf{x},t) = \nabla \cdot \mathbf{u}(e,\mathbf{x},t) \ , \tag{5}$$

$$\mathbf{S}(e,\mathbf{x},t) = \nabla \times \mathbf{u}(e,\mathbf{x},t) \ . \tag{6}$$

Equations 1-4 represent special cases of more general forms of extended imaging conditions (Rickett and Sava, 2002; Sava and Vasconcelos, 2009). An extended imaging condition defines the image as a function of space and cross-correlation lags, i.e., space-lag $\boldsymbol{\lambda}$ and time-lag τ:

$$I^{PP}(\mathbf{x},\boldsymbol{\lambda},\tau) = \sum_{e,t} P_s(\mathbf{x}-\boldsymbol{\lambda},t-\tau)\, P_r(\mathbf{x}+\boldsymbol{\lambda},t+\tau) \ , \tag{7}$$

$$I^{PS}(\mathbf{x},\boldsymbol{\lambda},\tau) = \sum_{e,t} \left[\nabla P_s(\mathbf{x}-\boldsymbol{\lambda},t-\tau) \times \mathbf{n}(\mathbf{x})\right] \cdot \mathbf{S}_r(\mathbf{x}+\boldsymbol{\lambda},t+\tau) \ , \tag{8}$$

$$I^{SP}(\mathbf{x},\boldsymbol{\lambda},\tau) = \sum_{e,t} \left[\nabla \times \mathbf{S}_s(\mathbf{x}-\boldsymbol{\lambda},t-\tau) \cdot \mathbf{n}(\mathbf{x})\right] P_r(\mathbf{x}+\boldsymbol{\lambda},t+\tau) \ , \tag{9}$$

$$I^{SS}(\mathbf{x},\boldsymbol{\lambda},\tau) = \sum_{e,t} \mathbf{S}_s(\mathbf{x}-\boldsymbol{\lambda},t-\tau) \cdot \mathbf{S}_r(\mathbf{x}+\boldsymbol{\lambda},t+\tau) \ . \tag{10}$$

Such extended images can be used in image post-processing for amplitude variation with angle analysis (Beretta et al., 2002), tomographic velocity analysis (Symes, 1993; Sava and Biondi, 2004; Yang and Sava, 2015), and artifacts attenuation (Zhang and Sun, 2008; Duan and Sava, 2014).

3 MOVEOUT ANALYSIS

The extended imaging condition in equations 7-10 preserve necessary information for decomposing images in angle-dependent components, which can be used for velocity analysis. In 3D, the PP, PS, SP, and SS images generated using this imaging condition are scalars, which can be used directly to extract angle gathers. We formulate our method under the assumption that the reflector is locally a plane, and that the incident and reflected wavefields are also locally planar. However, the derived algorithms are not limited to cases where the wavefronts are planar, because waves can always be decomposed to planar components, even in complex wavefields with triplicated waves.

We define the angle domain as the set of half-opening angle θ, and azimuth ϕ, and use the following unit vectors to describe the angle decomposition procedure (Figure 2):

- $\mathbf{o}$: azimuth vector acting as a reference direction, e.g., North
- $\mathbf{n}$: reflector normal
- $\mathbf{a}$: projection of the azimuth vector in the interface plane:

$$\mathbf{a} = (\mathbf{n} \times \mathbf{o}) \times \mathbf{n} \tag{11}$$

- $\mathbf{n}_s$: propagation direction of the incident wave
- $\mathbf{n}_r$: propagation direction of the reflected wave
- $\mathbf{q}$: vector lying at the intersection of the interface and the reflection plane:

$$\mathbf{q} = Q(\mathbf{n},\phi)\,\mathbf{a} \ , \tag{12}$$

where matrix $Q(\mathbf{n},\phi)$ is a rotation matrix defined by the axis

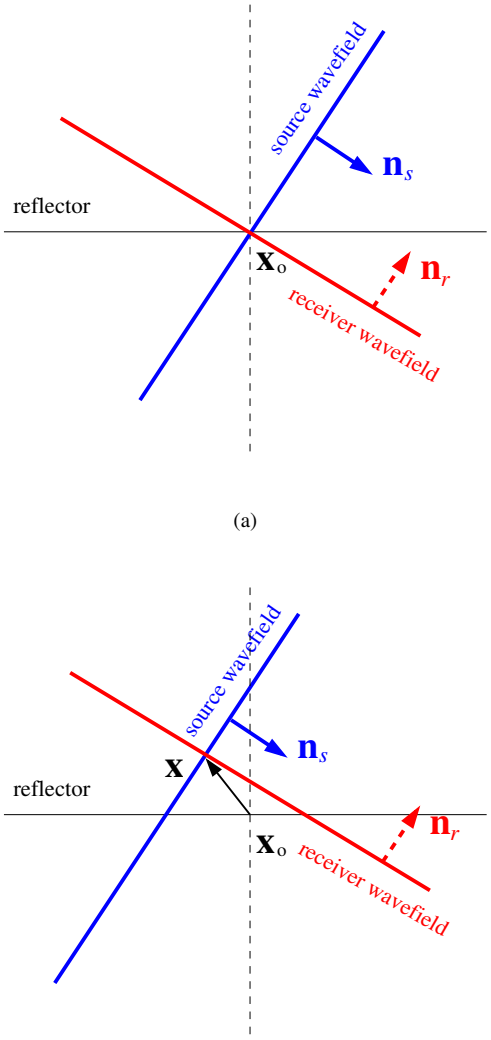


Figure 1. Cartoon describing source and receiver planes intersecting in the reflection plane (a) at location $\mathbf{x}_o$ at time t_o. (b) at location $\mathbf{x}$ after moving both planes along time- and space-axises. Vectors $\mathbf{n}_s$ and $\mathbf{n}_r$ define the propogation directions of the incident and reflected waves in space, respectively.

$\mathbf{n}$ and the angle ϕ:

$$Q=\begin{bmatrix} n_x^2+\left(n_y^2+n_z^2\right)\cos\phi & n_x n_y\,(1-\cos\phi)-n_z\sin\phi & n_x n_z\,(1-\cos\phi)+n_y\sin\phi \\ n_y n_x\,(1-\cos\phi)+n_z\sin\phi & n_y^2+\left(n_z^2+n_x^2\right)\cos\phi & n_y n_z\,(1-\cos\phi)-n_x\sin\phi \\ n_z n_x\,(1-\cos\phi)-n_y\sin\phi & n_z n_y\,(1-\cos\phi)+n_x\sin\phi & n_z^2+\left(n_x^2+n_y^2\right)\cos\phi \end{bmatrix} . \tag{13}$$

The (planar) source wavefield propagates along the direction indicated by vector $\mathbf{n}_s$ with speed v_s, and the (planar) receiver wavefield propagates along the direction indicated by vector $\mathbf{n}_r$ with speed v_r. As shown in Figure 1(a), the point of coordinates $\mathbf{x}_o$ indicates the location of the intersection of the two

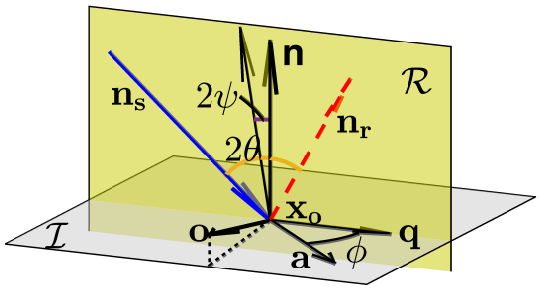


Figure 2. Schematic representation of the angles and vectors used in opening and azimuth angle decomposition for an image point $\mathbf{x}_o$. $\mathcal{I}$ and $\mathcal{R}$ are the interface plane and reflection planes, respectively. Vector $\mathbf{n}$ indicates the normal to the interface $\mathcal{I}$, vector $\mathbf{n}_s$ defines the propagation direction of the incident wave in space, vector $\mathbf{n}_r$ defines the propagation direction of the reflected wave in space, vector $\mathbf{a}$ is the projection of the azimuth vector in the interface plane, vector $\mathbf{o}$ is the reference direction, and vector $\mathbf{q}$ lies at the intersection of the interface and reflection planes. Angle 2θ is the sum of incidence and reflection angles, angle 2ψ is their difference, and angle ϕ is the azimuth.

wavefronts and the reflection plane at time $t = t_o$:

$$\begin{cases} \mathbf{n}_s \cdot (\mathbf{x} - \mathbf{x}_o) = v_s\,(t - t_o)\ , & (14) \\ \mathbf{n}_r \cdot (\mathbf{x} - \mathbf{x}_o) = v_r\,(t - t_o)\ . & (15) \end{cases}$$

Introducing time-lag τ and space-lag $\boldsymbol{\lambda}$ to equations 14 and 15 is equivalent to moving the wavefronts in time and space, respectively. After moving the wavefronts, the intersection of the two wavefronts in the reflection plane is shifted to position $\mathbf{x}$, as shown in Figure 1(b). The expressions for the extended imaging condition using the planar source and receiver wavefields are

$$\begin{cases} \mathbf{n}_s \cdot (\mathbf{x} - \mathbf{x}_o - \boldsymbol{\lambda}) = v_s\,(-\tau)\ , & (16) \\ \mathbf{n}_r \cdot (\mathbf{x} - \mathbf{x}_o + \boldsymbol{\lambda}) = v_r\,(+\tau)\ , & (17) \end{cases}$$

which can also be written as

$$\begin{cases} \left(\dfrac{\mathbf{n}_s}{v_s} - \dfrac{\mathbf{n}_r}{v_r}\right)\cdot(\mathbf{x}-\mathbf{x}_o) - \left(\dfrac{\mathbf{n}_s}{v_s} + \dfrac{\mathbf{n}_r}{v_r}\right)\cdot\boldsymbol{\lambda} = -2\tau\ , & (18) \\ \left(\dfrac{\mathbf{n}_s}{v_s} + \dfrac{\mathbf{n}_r}{v_r}\right)\cdot(\mathbf{x}-\mathbf{x}_o) - \left(\dfrac{\mathbf{n}_s}{v_s} - \dfrac{\mathbf{n}_r}{v_r}\right)\cdot\boldsymbol{\lambda} = 0\ , & (19) \end{cases}$$

where the vector $(\mathbf{x} - \mathbf{x}_o)$ measures the spatial shift of the image point, corresponding to time-lag τ and space-lag $\boldsymbol{\lambda}$.

We consider three types of extended images, using both space- and time-lags, or using time-lag, or using space-lags. For each extended image type we derive the equations that link space- or time-lag with half-opening angle θ and azimuth ϕ from equations 18 and 19. One common step for the three approaches is to replace vectors $\mathbf{n}_s$ and $\mathbf{n}_r$ with functions of vectors $\mathbf{n}$ and $\mathbf{q}$:

$$\begin{cases} \mathbf{n}_s = \mathbf{q}\sin(\theta - \psi) - \mathbf{n}\cos(\theta - \psi)\ , & (20) \\ \mathbf{n}_r = \mathbf{q}\sin(\theta + \psi) + \mathbf{n}\cos(\theta + \psi)\ . & (21) \end{cases}$$

As shown in Figure 2, the angle 2θ is the sum of the in-

cidence and reflection angles, and the angle 2ψ is their difference. Thus the incidence angle is $\theta - \psi$, and the reflection angle is $\theta + \psi$. With γ as the ratio of v_s and v_r, we use Snell's law and obtain the expression

$$\gamma = \frac{v_s}{v_r} = \frac{\sin(\theta - \psi)}{\sin(\theta + \psi)} , \tag{22}$$

or the expression for ψ using γ and θ:

$$\tan\psi = \frac{1-\gamma}{1+\gamma}\tan\theta . \tag{23}$$

By substituting equation 23 in equations 20 and 21, we can replace the angle ψ with a function of γ and θ. In the following derivation for angle decomposition, two expressions are frequently used:

$$\begin{cases} \mathbf{n}_s + \gamma\mathbf{n}_r = \dfrac{\left(\left(\gamma^2-1\right)\mathbf{n} + 2\mathbf{q}\gamma\sin 2\theta\right)}{\sqrt{\gamma^2+1+2\gamma\cos 2\theta}} , & (24) \\ \mathbf{n}_s - \gamma\mathbf{n}_r = -\mathbf{n}\sqrt{\gamma^2+1+2\gamma\cos 2\theta} . & (25) \end{cases}$$

3.1 Angle decomposition using CIPs

For CIP gathers, the relationships between time- and space-lags at point $\mathbf{x}_o$ using equations 18 and 19 are:

$$\begin{cases} \left(\dfrac{\mathbf{n}_s}{v_s} + \dfrac{\mathbf{n}_r}{v_r}\right)\cdot\boldsymbol{\lambda} = 2\tau , & (26) \\ \left(\dfrac{\mathbf{n}_s}{v_s} - \dfrac{\mathbf{n}_r}{v_r}\right)\cdot\boldsymbol{\lambda} = 0 . & (27) \end{cases}$$

Substituting equations 24 and 25 in equations 26 and 27, we obtain the system of equations that describes the relationships between image shift $(\mathbf{x} - \mathbf{x}_o)$ and time-lag τ:

$$\begin{cases} \dfrac{\gamma\sin 2\theta}{\sqrt{\gamma^2+1+2\gamma\cos 2\theta}}\left(\mathbf{q}\cdot\boldsymbol{\lambda}\right) = v_s\tau , & (28) \\ \mathbf{n}\cdot\boldsymbol{\lambda} = 0 . & (29) \end{cases}$$

The pseudocode for angle decomposition procedure using time- and space CIP gathers (equations 28 and 29) is shown in Algorithm 1. Given the normal vector $\mathbf{n}$ and the azimuth reference vector $\mathbf{o}$, we compute vector $\mathbf{a}$, which is the projection of the azimuth vector in the interface plane. Then, we loop over all possible values of the azimuth angle ϕ and construct the vector $\mathbf{q}$, which lies at the intersection of the interface and the reflection planes. This step is a rotation of the azimuth reference vector $\mathbf{a}$ within the interface plane by the azimuth angle ϕ. Next, we loop over all possible values of the reflection angle θ and apply a slant-stack to $\mathbf{I}(\boldsymbol{\lambda},\tau)$ using equations 28 and 29. The output image $\mathbf{I}(\phi,\theta)$ is a function of half-opening angle θ and azimuth angle ϕ.

Equations 28 and 29 simplify to the acoustic case, with velocity ratio $\gamma = 1$ (Sava and Vlad, 2011):

$$\begin{cases} \sin\theta\left(\mathbf{q}\cdot\boldsymbol{\lambda}\right) = v_s\tau , & (30) \\ \mathbf{n}\cdot\boldsymbol{\lambda} = 0 . & (31) \end{cases}$$

We illustrate this angle decomposition methodology using a simple example. The model is homogeneous with a horizontal reflector in P velocity, as shown in Figure 3. The acquisition geometry contains a source at $\{0.4, 0.4, 0.02\}$ km and a 2D network of receivers at $z = 0.02$ km. We generate a three-component shot gather using a vertical displacement source with a 110Hz peak frequency Ricker wavelet. Figures 4 and 7 show the PP and PS images, respectively, which are computed using the imaging condition shown in equations 1 and 2. Both the PP and PS images are scalars without polarity reversal. Figure 5(a) shows a PP CIP gather at coordinates $\{0.33, 0.33, 0.2\}$ km. Following Algorithm 1, we compute the corresponding angle gather shown in Figure 5(b). The dot overlain on the angle gather indicates the analytical estimation of the opening and azimuth angle using the acquisition geometry. We also compute PP angle gathers for eight different shots, shown in Figure 6(a). Because the migration velocity is correct, the summation of the eight extended PP images forms a focusing point at $\tau = 0$, $\boldsymbol{\lambda} = \mathbf{0}$. Figure 6(b) shows the combination of eight PP angle gathers at the center of the reflector, which match the analytical estimation shown as dots. Similarly, we compute the PS angle gather (Figure 8(b)) for the CIP gather (Figure 8(a)) at coordinates $\{0.2, 0.2, 0.2\}$ km. Figure 9(b) shows the combination of eight PS angle gathers for eight different shots (Figure 9(a)). These examples demonstrate the accuracy of the angle decomposition algorithm.

Algorithm 1 Isotropic angle decomposition using time- and space-lag CIP gathers

```
for each CIP do
    input I(λ, τ)
    input n, o, γ, v_s
    {n, o} → a
    for φ = 0° ... 360° do
        {n, a, φ} → q
        for θ = 0° ... 90° do
            I(λ, τ) ⟹ I(φ, θ)
        end for
    end for
    return I(φ, θ)
end for
```

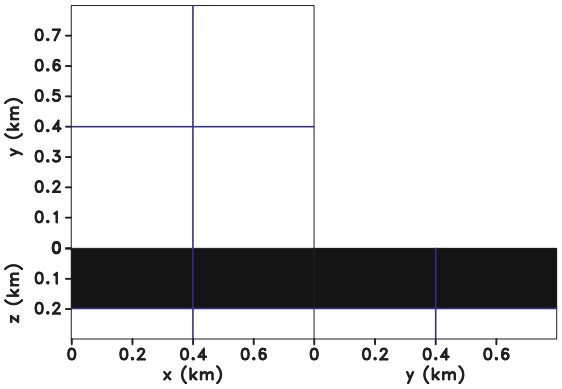


Figure 3. 3D P velocity model with one horizontal reflector at $z = 0.2$ km in a homogeneous medium.

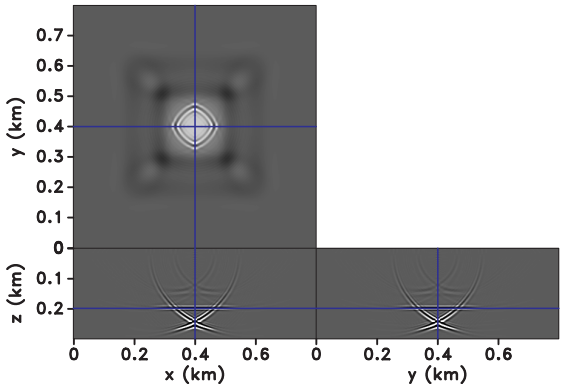
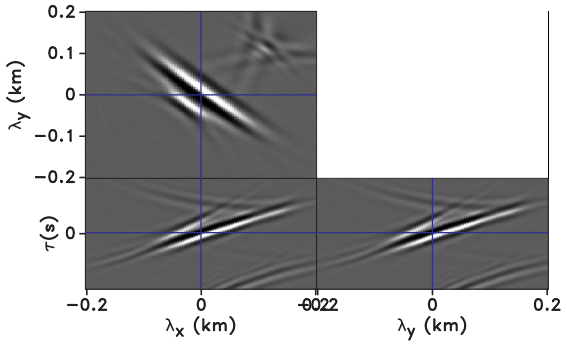
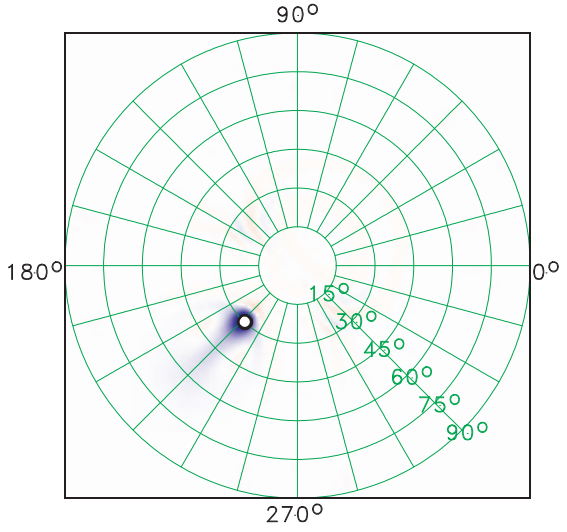


Figure 4. The PP image computed from one shot gather.

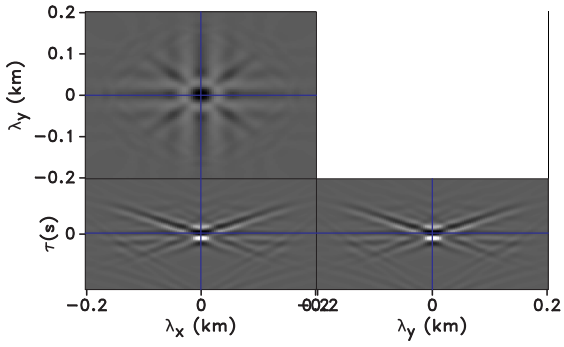


(a)

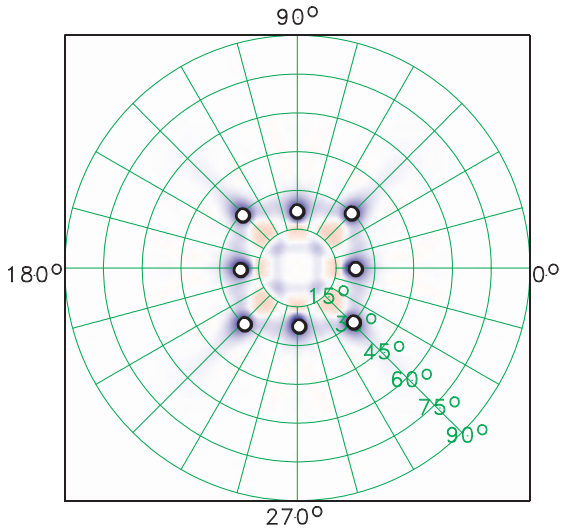


(b)

Figure 5. (a) Extended CIP and (b) wide-azimuth angle gather the PP image at coordinates $\{0.33, 0.33, 0.2\}$ km. The dot represents the analytical estimation of the opening and azimuth angle using the acquisition geometry.



(a)



(b)

Figure 6. (a) Combination of eight PP extended CIP gathers at the same location from eight shots. (b) combination of eight PP angle gathers. The dots represent the analytical estimations of the opening and azimuth angles using the acquisition geometry.

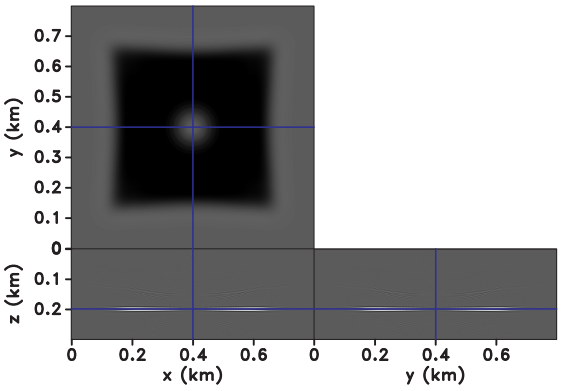
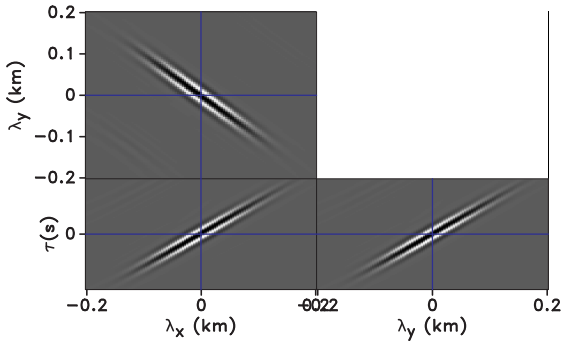
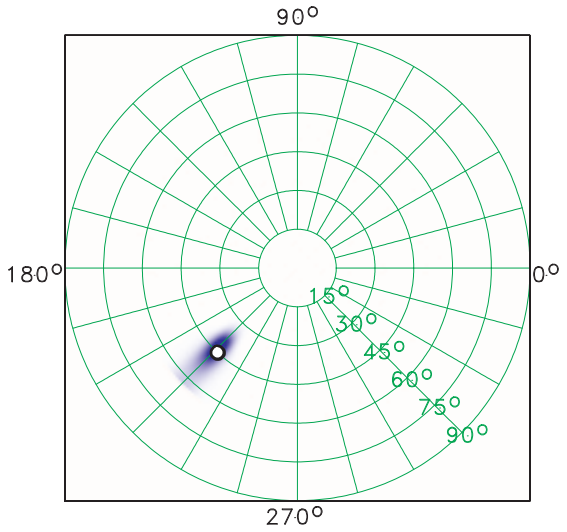


Figure 7. The PS image computed from one shot gather.

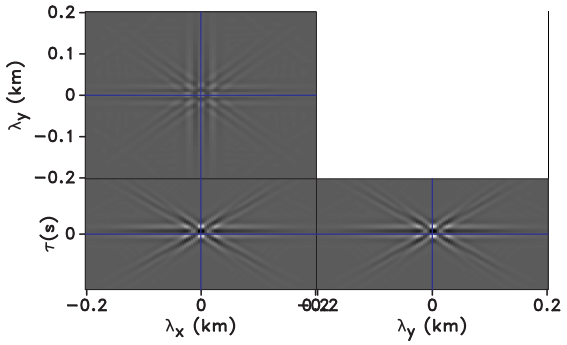


(a)

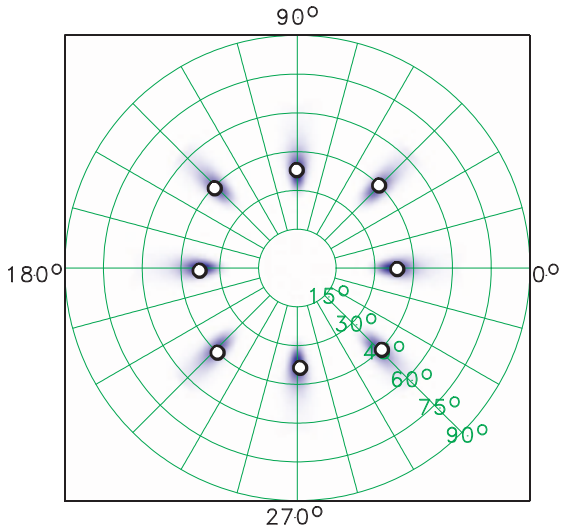


(b)

Figure 8. (a) Extended CIP and (b) wide-azimuth angle gather for the PS image at coordinates $\{0.2, 0.2, 0.2\}$ km. The dot represents the analytical estimation of the opening and azimuth angle using the acquisition geometry.



(a)



(b)

Figure 9. (a) Combination of eight PS extended CIP gathers at the same location from eight shots. (b) combination of eight PS angle gathers. The dots represent the analytical estimations of the opening and azimuth angles using the acquisition geometry.

3.2 Angle decomposition using τCIGs

For time-lag common image gathers (τCIGs), we set $\boldsymbol{\lambda} = \mathbf{0}$ in equations 18 and 19 and obtain

$$\begin{cases} \left(\dfrac{\mathbf{n}_s}{v_s} - \dfrac{\mathbf{n}_r}{v_r}\right) \cdot (\mathbf{x} - \mathbf{x}_o) + 2\tau = 0 \ , & (32) \\ \left(\dfrac{\mathbf{n}_s}{v_s} + \dfrac{\mathbf{n}_r}{v_r}\right) \cdot (\mathbf{x} - \mathbf{x}_o) = 0 \ , & (33) \end{cases}$$

which show the relationships between image shift $(\mathbf{x} - \mathbf{x}_o)$ and time-lag τ.

Substituting equations 24 and 25 in equations 32 and 33, we obtain the system for angle decomposition using time-lag extended images:

$$\begin{cases} \dfrac{\sqrt{\gamma^2+1+2\gamma\cos 2\theta}}{2}[\mathbf{n}\cdot(\mathbf{x}-\mathbf{x}_o)] = v_s\tau \ , & (34) \\ \sin 2\theta\sqrt{\gamma^2+1+2\gamma\cos 2\theta}[\mathbf{q}\cdot(\mathbf{x}-\mathbf{x}_o)] = v_s\tau\left(\dfrac{1}{\gamma}-\gamma\right) \ , & (35) \end{cases}$$

where equation 34 corresponds to the projection of the image shift $(\mathbf{x} - \mathbf{x}_o)$ on the reflector normal $\mathbf{n}$, and equation 35 corresponds to the projection of the image shift $(\mathbf{x} - \mathbf{x}_o)$ on vector $\mathbf{q}$. Algorithm 2 shows the pseudocode for the angle decomposition procedure using space-lag extended images. Given normal vector $\mathbf{n}$, velocity ratio γ, and incident wave velocity v_s, we loop over all possible values of the azimuth angle ϕ and construct the vector $\mathbf{q}$, which lies at the intersection of the interface and the reflection plane. Next, we loop over all

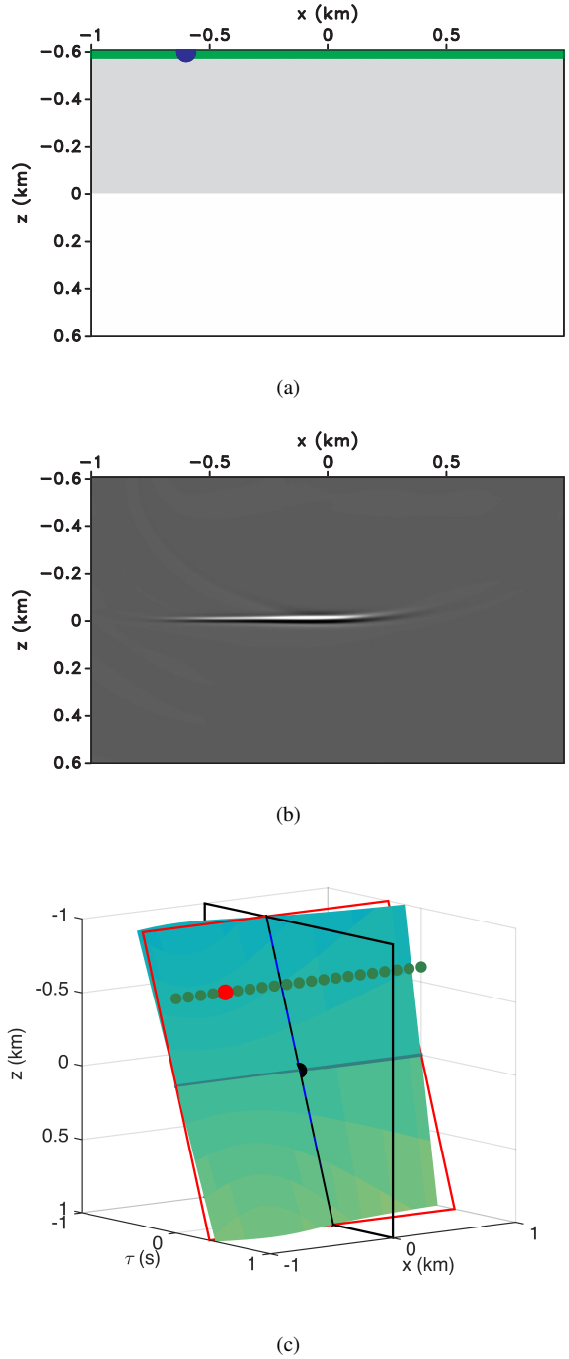


Figure 10. (a) 2D P-velocity model with a horizontal reflector at $z = 0.0$ km. The dot represents the source location, and the line represents the receiver locations. (b) PP image computed from one shot gather. (c) Predicted spatial shift of a horizontal reflector for $\gamma = 1$. The dot at coordinates $x = -0.6$ km, $z = -0.6$ km, $\tau = 0$ s represents the source location, and the line at $z = -0.6$ km, $\tau = 0$ s represents the receiver locations. The line at $z = 0.0$ km, $\tau = 0$ s shows the zero-lag image. The black line illustrates the spatial shift for the image point at $\{0.0, 0.0\}$ km, which is along the z axis in the model space,

possible values of the opening angle θ and azimuth angle ϕ, and apply a slant-stack along the surface described in equations 34 and 35 to the extended image $\mathbf{I}(\mathbf{x}, \tau)$. The output is image $\mathbf{I}(\mathbf{x}, \phi, \theta)$ as a function of space location $\mathbf{x}$, angle θ, and angle ϕ.

Algorithm 2 Elastic angle decomposition using τCIGs

for each τCIG **do**
  input $\mathbf{I}(\mathbf{x}, \tau)$
  input $\mathbf{n}$, $\mathbf{o}$, γ, v_s
  $\{\mathbf{n}, \mathbf{o}\} \rightarrow \mathbf{a}$
  for $\phi = 0^\circ \ldots 360^\circ$ **do**
    $\{\mathbf{n}, \mathbf{a}, \phi\} \rightarrow \mathbf{q}$
    for $\theta = 0^\circ \ldots 90^\circ$ **do**
      $\mathbf{I}(\mathbf{x}, \tau) \Longrightarrow \mathbf{I}(\mathbf{x}, \phi, \theta)$
    end for
  end for
  return $\mathbf{I}(\mathbf{x}, \phi, \theta)$
end for

Equations 34 and 35 simplify to the acoustic case, with velocity ratio $\gamma = 1$ (Sava and Fomel, 2006):

$$\begin{cases} \cos\theta\,[\mathbf{n} \cdot (\mathbf{x} - \mathbf{x}_o)] = v_s \tau\ , & (36) \\ \mathbf{q} \cdot (\mathbf{x} - \mathbf{x}_o) = 0\ . & (37) \end{cases}$$

Note that in equations 36 and 37, time-lag τ is not related to the azimuth vector $\mathbf{q}$, i.e., time-lag extended images do not contain azimuthal information for the acoustic case. However, for converted waves ($\gamma \neq 1$), time-lag extended images contain azimuthal information, according to equations 34 and 35.

We illustrate this algorithm with 2D examples. Figure 10(a) shows a two layered model with a horizontal reflector in the P-velocity model. The acquisition geometry contains one source, at $\{-0.6, -0.6\}$ km, and one receiver line, at $z = -0.6$ km. The computed PP image is shown in Figure 10(b). Using equations 36 and 37, we can predict the spatial shift of the reflector as function of time-lag τ and space $\mathbf{x}$, shown in Figure 10(c). Because the opening angle for each image point on the reflector changes with its relative position to the source, the spatial shift for each image point also varies. Figure 13(a) shows the computed extended image gathers at several x locations, indicated by the number below each image panel. The shapes of the extended images in each panel are straight lines, which matches the corresponding vertical slice of the surface in Figure 10(c). We compare the angle gathers at those x locations, computed using the algorithm that maps each vertical time-lag gather individually to a angle gather, with the angle gathers computed using the method shown in Algorithm 2, which applies a slant-stack along the surface shown in Figure 10(c). Because the image shifts vertically in the time-lag gather for this example, the two methods generate similar angle gathers.

Figure 11(a) shows a two layered model with a dipping reflector in P velocity. The computed PP image is shown in Figure 11(b). Using equations 36 and 37, we can predict the spatial shift of the reflector as a function of time-lag τ, shown in Figure 11(c). The dashed line is the intersection of two

planes (equations 36 and 37), which illustrates the spatial shift for image point at $x = 0.0$ km, $z = -0.6$ km. The solid line through the image point at $x = 0.0$ km, $z = 0.0$ km which shows a vertical CIG. Note that the two lines do not coincide with each other, i.e., the method that applies a line slant-stack to the vertical trace does not measure the spatial image shift $(\mathbf{x} - \mathbf{x}_o)$ accurately. The angle gathers computed using this method and the one in Algorithm 2 are shown in Figures 14(b) and 14(c), respectively.

For converted waves, the image does not only shift vertically but also horizontally in the time-lag gather even for a horizontal reflector. Figure 12(a) shows a two layered model with a horizontal reflector in P velocity. Figure 12(b) is the computed PS image, using the scalar imaging condition (equation 2). The predicted spatial shift of the reflector is shown in Figure 12(c). Figure 13(a) shows the computed extended image gathers at several x locations. Note that the shape of the image in each panel is a curved line. We compare the angle gathers at those x locations, computed using the algorithm that applies a line slant-stack to each image panel (Figure 13(b)), with the angle gathers computed using the method shown in Algorithm 2 (Figure 13(c)), which applies a slant-stack along the surface shown in Figure 10(c). Using the surface slant-stack, we obtain more focused angle gathers.

4 ANGLE DECOMPOSITION USING λCIG

For space-lag extended images (λCIGs), we set $\tau = 0$ in equations 18 and 19 and obtain

$$\left\{ \begin{array}{l} \left(\dfrac{\mathbf{n}_s}{v_s} - \dfrac{\mathbf{n}_r}{v_r}\right) \cdot (\mathbf{x} - \mathbf{x}_o) = \left(\dfrac{\mathbf{n}_s}{v_s} + \dfrac{\mathbf{n}_r}{v_r}\right) \cdot \boldsymbol{\lambda} \,, \quad (38) \\ \left(\dfrac{\mathbf{n}_s}{v_s} + \dfrac{\mathbf{n}_r}{v_r}\right) \cdot (\mathbf{x} - \mathbf{x}_o) = \left(\dfrac{\mathbf{n}_s}{v_s} - \dfrac{\mathbf{n}_r}{v_r}\right) \cdot \boldsymbol{\lambda} \,, \quad (39) \end{array} \right.$$

which show the relationships between image shifts $(\mathbf{x} - \mathbf{x}_o)$ and space-lag $\boldsymbol{\lambda}$.

Substituting equations 24 and 25 in equations 38 and 39, we obtain

$$\left\{ \begin{array}{l} \dfrac{\gamma^2+1+2\gamma\cos 2\theta}{2\gamma} \mathbf{n}\cdot(\mathbf{x}-\mathbf{x}_o) + \sin 2\theta \mathbf{q}\cdot\boldsymbol{\lambda} = \dfrac{1-\gamma^2}{2\gamma}\mathbf{n}\cdot\boldsymbol{\lambda} \,, \quad (40) \\ \dfrac{\gamma^2+1+2\gamma\cos 2\theta}{2\gamma} \mathbf{n}\cdot\boldsymbol{\lambda} + \sin 2\theta \mathbf{q}\cdot(\mathbf{x}-\mathbf{x}_o) = \dfrac{1-\gamma^2}{2\gamma}\mathbf{n}\cdot(\mathbf{x}-\mathbf{x}_o) \,. \quad (41) \end{array} \right.$$

The terms $\mathbf{n} \cdot (\mathbf{x} - \mathbf{x}_o)$ and $\mathbf{q} \cdot (\mathbf{x} - \mathbf{x}_o)$ are projections of vector $(\mathbf{x} - \mathbf{x}_o)$ to the normal vector $\mathbf{n}$ and azimuth vector $\mathbf{q}$, respectively. Algorithm 3 shows the pseudocode for the angle decomposition procedure using space-lag extended images. Given normal vector $\mathbf{n}$ and azimuth reference vector $\mathbf{o}$, we compute vector $\mathbf{a}$, and loop over all possible values of the azimuth angle ϕ and construct the vector $\mathbf{q}$, which lies at the intersection of the interface and reflection plane. This step is a rotation of the azimuth reference vector $\mathbf{a}$ within the interface plane by angle ϕ. Next, we loop over all possible values of the reflection angle θ and apply a slant-stack along the surface de-

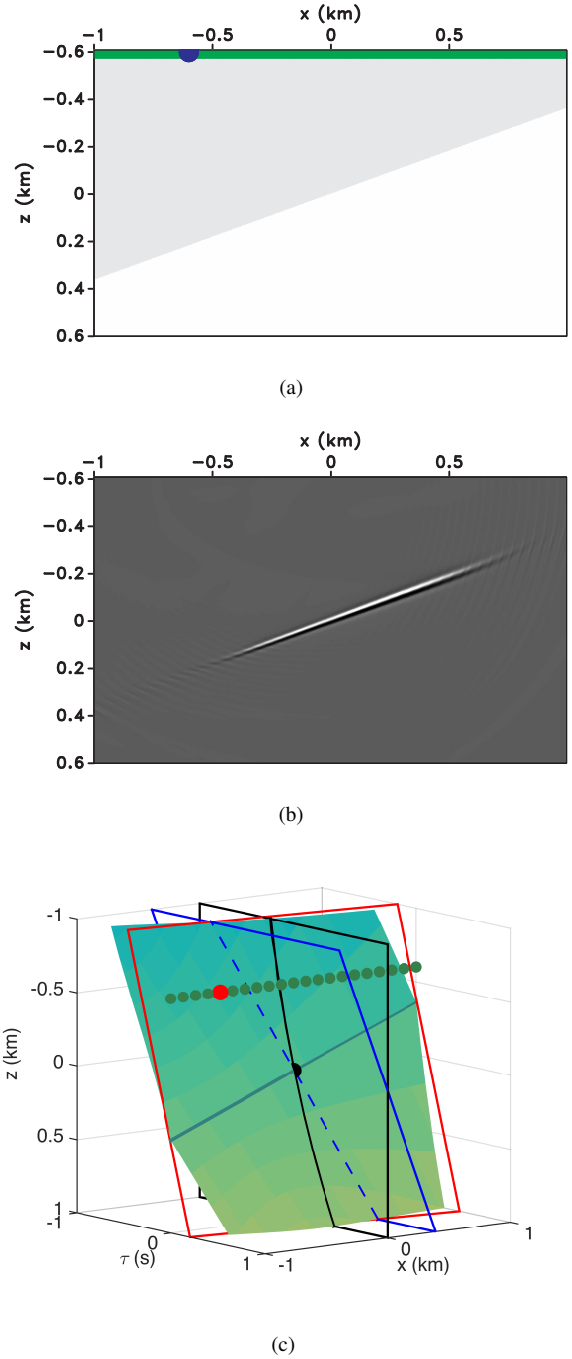
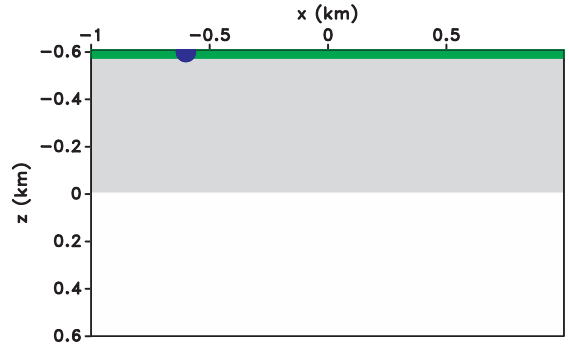
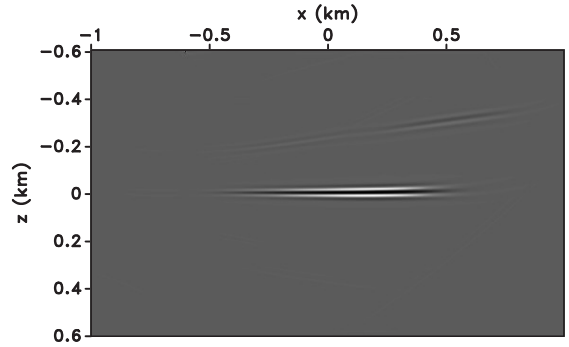


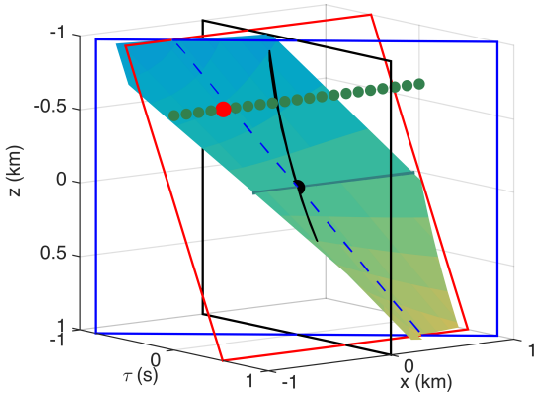
Figure 11. (a) 2D P-velocity model with a dipping reflector. The dot represents the source location, and the line represents the receiver locations. (b) PP image computed from one shot gather. (c) Predicted spatial shift of a dipping reflector for $\gamma = 1$. The dot at coordinates $x = -0.6$ km, $z = -0.6$ km, $\tau = 0$ s represents the source location, and the line at $z = -0.6$ km, $\tau = 0$ s represents the receiver locations. The line at $z = 0.0$ km, $\tau = 0$ s shows the zero-lag image. The dashed line illustrates the spatial shift for image point at $\{0.0, -0.6\}$ km, The vertical line illustrates the extended image for a time-lag gather at a fixed hozitontal position ($x = 0.0$ km). Note that these two lines do not overlay.



(a)



(b)



(c)

Figure 12. 2D elastic model with a horizontal reflector in the P-velocity model. the dot represents the source location, and the line represents the receiver locations. (b) PS image computed from one shot gather. (c) Predicted spatial shift of a horizontal reflector for $\gamma = 1.8$. The dot at coordinates $x = -0.6$ km, $z = -0.6$ km, $\tau = 0$ s represents the source location, and the line at $z = -0.6$ km, $\tau = 0$ s represents the receiver locations. The line at $z = 0.0$ km, $\tau = 0$ s shows the zero-lag image. The dashed line illustrates the spatial shift for image point at $\{0.0, -0.6\}$ km, The vertical line illustrates the extended image for a time-lag gather at a fixed horizontal position ($x = 0.0$ km). Note that these two lines do not overlay.

scribed in equations 40 and 41 to the extended image $\mathbf{I}(\mathbf{x}, \boldsymbol{\lambda})$. The output is image $\mathbf{I}(\mathbf{x}, \phi, \theta)$ as a function of half-opening angle θ and azimuth angle ϕ.

Algorithm 3 Elastic angle decomposition using λCIGs

for each λCIG **do**
  input $\mathbf{I}(\mathbf{x}, \boldsymbol{\lambda})$
  input $\mathbf{n}$, $\mathbf{o}$, γ
  $\{\mathbf{n}, \mathbf{o}\} \rightarrow \mathbf{a}$
  for $\phi = 0^\circ \ldots 360^\circ$ **do**
    $\{\mathbf{n}, \mathbf{a}, \phi\} \rightarrow \mathbf{q}$
    for $\theta = 0^\circ \ldots 90^\circ$ **do**
      $\mathbf{I}(\mathbf{x}, \boldsymbol{\lambda}) \Longrightarrow \mathbf{I}(\mathbf{x}, \phi, \theta)$
    end for
  end for
  return $\mathbf{I}(\mathbf{x}, \phi, \theta)$
end for

Equations 40 and 41 simplify to the acoustic case, with velocity ratio $\gamma = 1$:

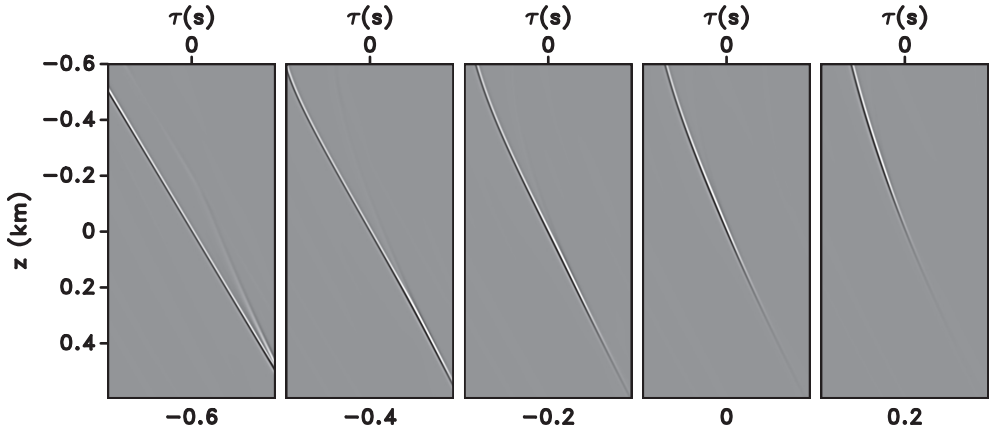
$$\begin{cases} \mathbf{n} \cdot (\mathbf{x} - \mathbf{x}_o) + \tan\theta\,(\mathbf{q} \cdot \boldsymbol{\lambda}) = 0\,, & (42) \\ \tan\theta\,[\mathbf{q} \cdot (\mathbf{x} - \mathbf{x}_o)] + (\mathbf{n} \cdot \boldsymbol{\lambda}) = 0\,, & (43) \end{cases}$$

where equation 42 is first proposed by Sava and Fomel (2005).

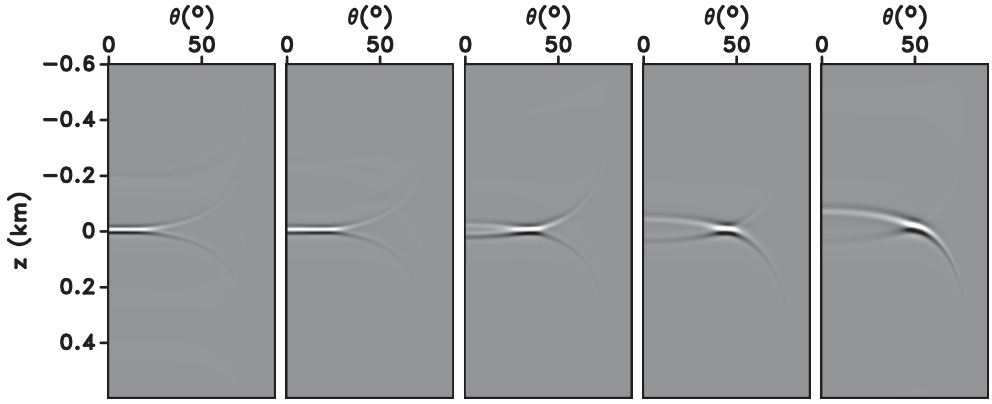
5 EXAMPLES

For simple geologic models, subsurface illumination from different angles tends to be uniform. However, in areas with complex geologic structures such as salt bodies, severe wavefield distortions lead to irregular subsurface illumination patterns, even if acquisition distribution is uniform. Angle gathers can provide indication of subsalt illumination, which benefits reservoir characterization and acquisition design.

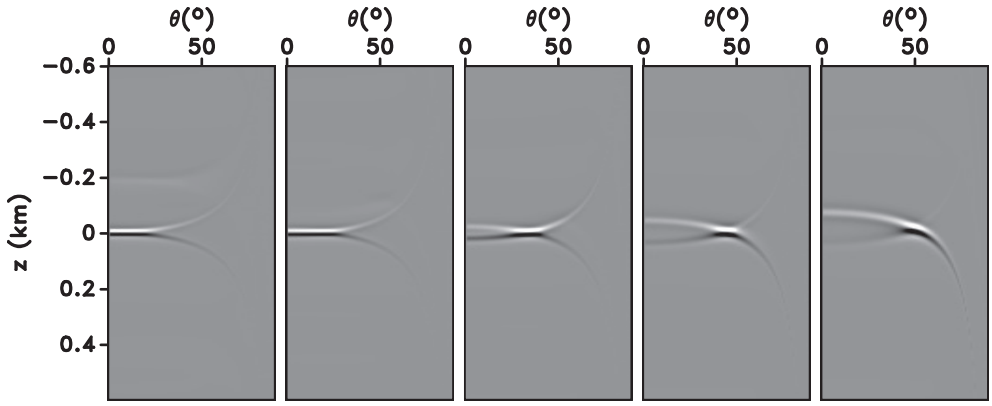
We show angle gather computed using the proposed elastic angle decomposition methodologes for the SEG/EAGE salt model (Aminzadeh et al., 1996), shown in Figure 16(a). We add a horizontal reflector at $z = 0.3$ km, and compute the angle and azimuth for a image point on the horizontal reflector at coordinates $x = 0.3$ km, $y = 0.4$ km. The acquisition geometry consists of 91 sources and a 2D network of receivers at z = 0.02 km. We generate three-component shot gathers using a vertical displacement source with a 100Hz peak frequency Ricker wavelet. As shown in Figure 16(b), due to the existence of the salt body above the horizontal reflector, it is hard to obtain illumination at the highlighted subsurface image point, at coordinates $x = 0.3$ km, $y = 0.4$ km, from certain azimuth ranges. We define azimuth $\phi = 90^\circ$ as North. Figures 17(b) and 18(b) show the stacked angle and azimuth gather at coordinates $x = 0.3$ km, $y = 0.4$ km, $z = 0.3$ km, which are computed from PP and PS CIP gathers, respectively, using Algorithm 1. Both angle gathers show similar illumination patterns. For the PP image, this image point is mainly illuminated from the west direction, and for the PS image, this image point is illuminated from the west and the south direc-



(a)



(b)



(c)

Figure 13. (a) Computed extended image gathers at several x-location, indicated by the number below each image. The shape of the image in each panel matches the corresponding horizontal slice of the surface plot in Figure 10(c). Computed angles for all samples on the reflector by applying (b) a line slant-stack along the vertical trace, and (c) the method described in Algorithm 2, which applies a slant-stack along the surface shown in Figure 10(c). The two methods generate similar angle gathers.

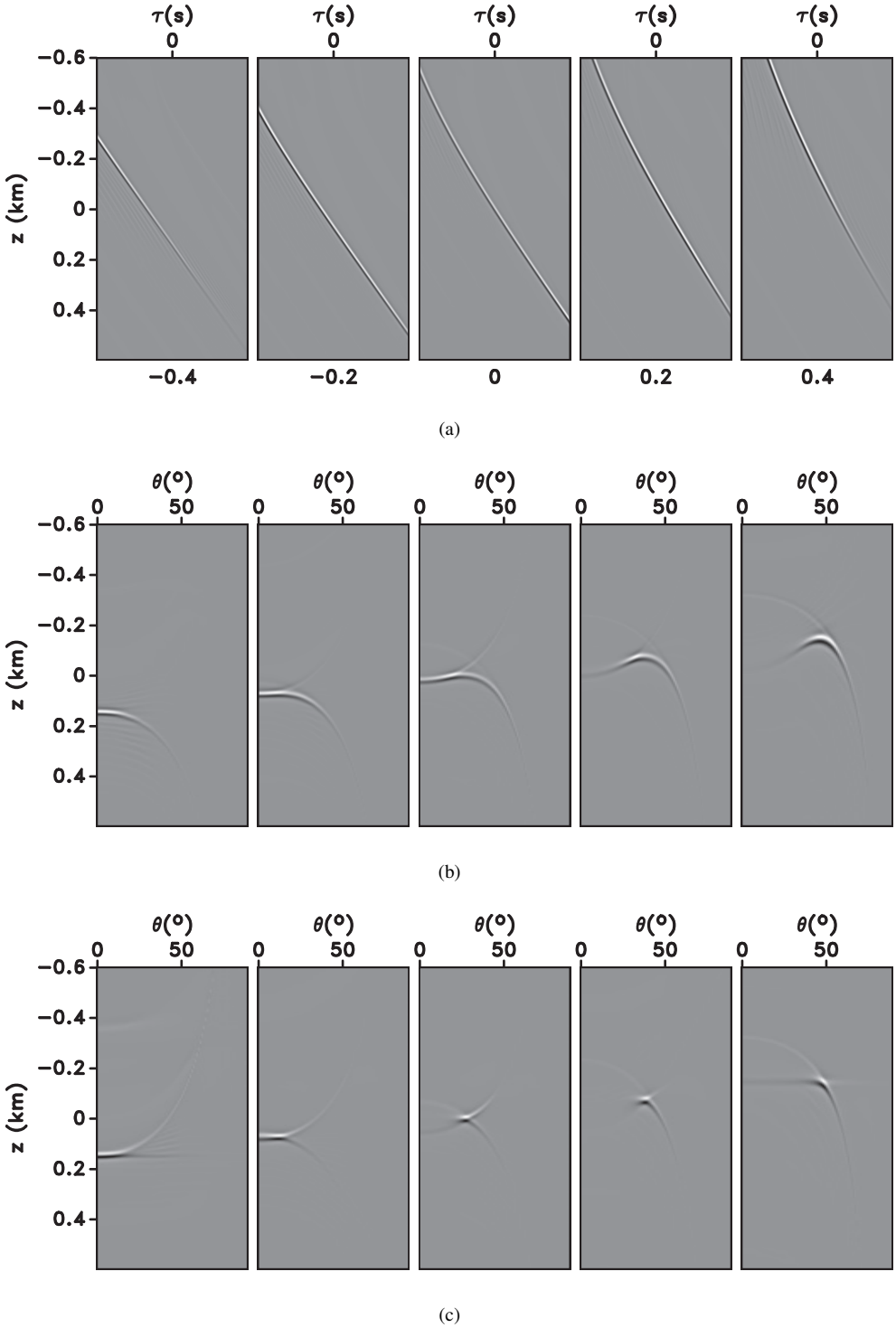
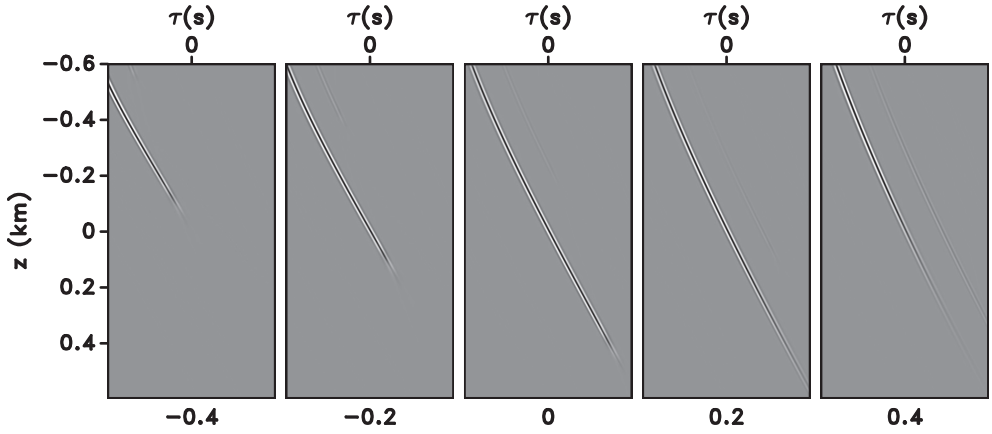
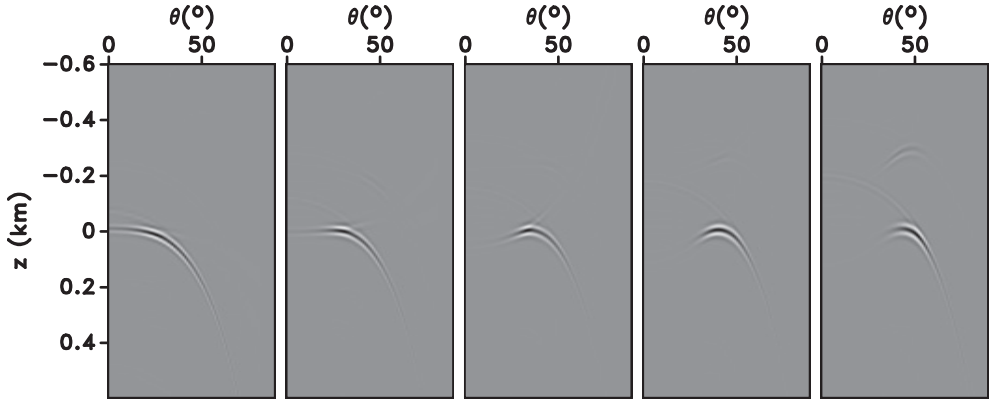


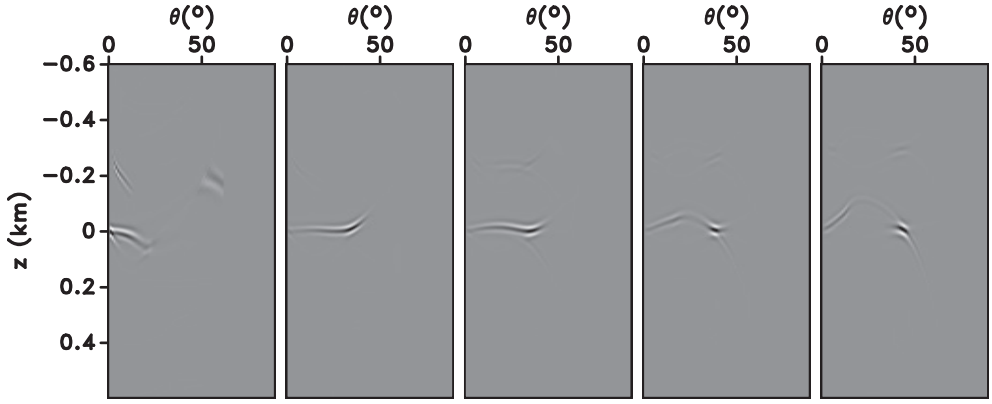
Figure 14. (a) Computed extended image gathers at several x-location, indicated by the number below each image. The shape of the image in each panel matches the corresponding horizontal slice of the surface plot in Figure 11(c). Computed angles for all samples on the reflector by applying (b) a line slant-stack along the vertical trace, and (c) the method described in Algorithm 2, which applies a slant-stack along the surface shown in Figure 11(c). The angle gathers in (c) are more focused.



(a)



(b)



(c)

Figure 15. (a) Computed extended image gathers at several x-location, indicated by the number below each image. The shape of image in each panel matches the corresponding horizontal slice of the surface plot in Figure 12(c). Computed angles for all samples on the reflector by applying (b) a line slant-stack along the vertical trace, and (c) the method described in Algorithm 2, which applies a surface slant-stack along the surface shown in Figure 12(c). The angle gathers in (c) are more focused.

tions. Compared to the PP angle gather, the PS angle gather in general has higher resolution.

6 CONCLUSIONS

Elastic 3D angle gathers can be computed from time-lag or space-lag common image gathers, as well as from mixed time-/space-lag common image point gathers. We propose extended imaging conditions to compute scalar PP, PS, SP, and SS images, from which we developed algorithms to compute opening and azimuth angle gathers. Angle gathers obtained using our algorithms, which convert from common image or common image point gathers by slant-stacking along surfaces within the gathers, are more accurate compare to those obtained by the more conventional approach of slant-stacking along lines. In addition, the methods using time-lag or space-lag common image gathers map all image points simultaneously from the model space to the angle domain, which results in similar computational cost compared to methods that utilize slant-stacks along lines in individual common image gathers. Examples in both 2D and 3D demonstrate that our methods correctly handles dipping reflectors as well as converted wave images. The computed angle gathers correctly indicate the illumination pattern for subsurface image points, which is important for acquisition design and reservoir characterization.

7 ACKNOWLEDGMENTS

We thank sponsors of the Center for Wave Phenomena, whose support made this research possible. The reproducible numeric examples in this paper use the Madagascar open-source software package (Fomel et al., 2013) freely available from http://www.ahay.org. The authors thank Paul Fowler for helpful discussions and valuable suggestions.

REFERENCES

Aminzadeh, F., N. Burkhard, J. Long, T. Kunz, and P. Duclos, 1996, Three dimensional SEG/EAEG models-an update: The Leading Edge, **15**, 131–134.

Audebert, F., P. Froidevaux, I. Huard, L. Nicoletis, and J. Svay-Lucas, 2000, A multi-angle toolbox for restored amplitude images and ava-gathers: 70th Ann. Internat. Mtg. Soc. of Expl. Geophys, **1023**.

Beretta, M. M., G. Bernasconi, and G. Drufuca, 2002, AVO and AVA inversion for fractured reservoir characterization: Geophysics, **67**, 300–306.

Biondi, B., and W. W. Symes, 2004, Angle-domain common-image gathers for migration velocity analysis by wavefield-continuation imaging: Geophysics, **69**, 1283–1298.

Brandsberg-Dahl, S., M. V. de Hoop, and B. Ursin, 1999, Velocity analysis in the common scattering-angle/azimuth domain: 69th SEG meeting, Houston, USA, Expanded Abstracts, 1222–1223.

De Bruin, C., C. Wapenaar, and A. Berkhout, 1990, Angle-dependent reflectivity by means of prestack migration: Geophysics, **55**, 1223–1234.

Dellinger, J., and J. Etgen, 1990, Wave-field separation in two-dimensional anisotropic media: Geophysics, **55**, 914–919.

Duan, Y., and P. Sava, 2015, Scalar imaging condition for elastic reverse time migration: Geophysics, **80**, S127–S136.

Duan, Y., and P. C. Sava, 2014, Elastic reverse-time migration with OBS multiples: SEG Technical Program Expanded Abstracts, 4071–4076.

Fomel, S., P. Sava, I. Vlad, Y. Liu, and V. Bashkardin, 2013, Madagascar: open-source software project for multidimensional data analysis and reproducible computational experiments: Journal of Open Research Software, **1**, e8.

Patrikeeva, N., and P. Sava, 2013, Comparison of angle decomposition methods for wave-equation migration: Presented at the 2013 SEG Annual Meeting, Society of Exploration Geophysicists.

Rickett, J. E., and P. C. Sava, 2002, Offset and angle-domain common image-point gathers for shot-profile migration: Geophysics, **67(3)**, 883–889.

Sava, P., 2007, Stereographic imaging condition for wave-equation migration: Geophysics, **72**, A87–A91.

Sava, P., and T. Alkhalifah, 2013, Wide-azimuth angle gathers for anisotropic wave-equation migration: Geophysical Prospecting, **61**, 75–91.

Sava, P., and B. Biondi, 2004, Wave-equation migration velocity analysis. I. Theory: Geophysical Prospecting, **52**, 593–606.

Sava, P., and S. Fomel, 2005, Coordinate-independent angle-gathers for wave equation migration: Presented at the 2005 SEG Annual Meeting, Society of Exploration Geophysicists.

———, 2006, Time-shift imaging condition in seismic migration: Geophysics, **71**, S209–S217.

Sava, P. C., and S. Fomel, 2003, Angle-domain common-image gathers by wavefield continuation methods: Geophysics, **68(3)**, 1065–1074.

Sava, P. C., and I. Vasconcelos, 2009, Efficient computation of extended images by wavefield-based migration: SEG Technical Program Expanded Abstracts 2009, 2824–2828.

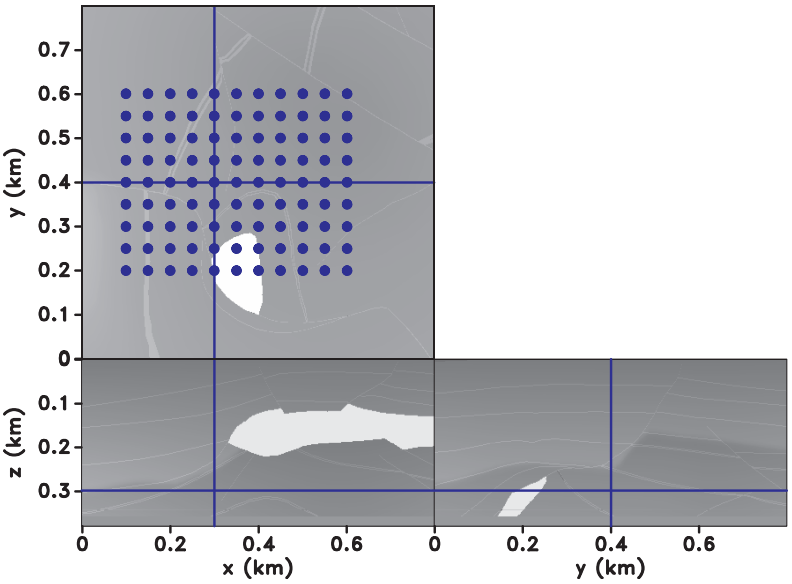
Sava, P. C., and I. Vlad, 2011, Wide-azimuth angle gathers for wave-equation migration: Geophysics, **76(3)**, S131–S141.

Symes, W. W., 1993, A differential semblance criterion for inversion of multioffset seismic reflection data: Journal of Geophysical Research: Solid Earth, **98**, 2061–2073.

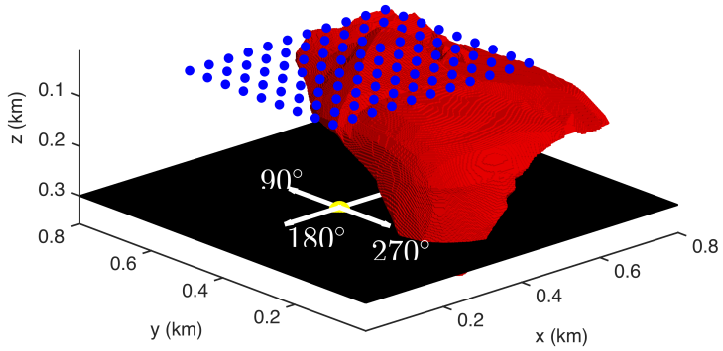
Vyas, M., X. Du, E. Mobley, and R. Fletcher, 2011, Methods for computing angle gathers using RTM: Presented at the 73rd EAGE Conference & Exhibition.

Wu, R.-S., and X.-B. Xie, 2002, Extracting angle domain information from migrated wavefield: Presented at the 2002 SEG Annual Meeting, Society of Exploration Geophysicists.

Xu, S., H. Chauris, G. Lambaré, and M. Noble, 2001, Common-angle migration: A strategy for imaging complex



(a)



(b)

Figure 16. (a) SEG/EAGE model. The dots show the source locations. (b) Relative position of the image point and the salt body.

media: Geophysics, **66**, 1877–1894.

Xu, S., Y. Zhang, and B. Tang, 2011, 3D angle gathers from reverse time migration: Geophysics, **76(2)**, S77–S92.

Yan, J., and W. Ross, 2013, Improving the stability of angle gather computation using Poynting vectors: Presented at the 2013 SEG Annual Meeting, Society of Exploration Geophysicists.

Yan, J., and P. Sava, 2008, Isotropic angle-domain elastic reverse-time migration: Geophysics, **73(6)**, S229–S239.

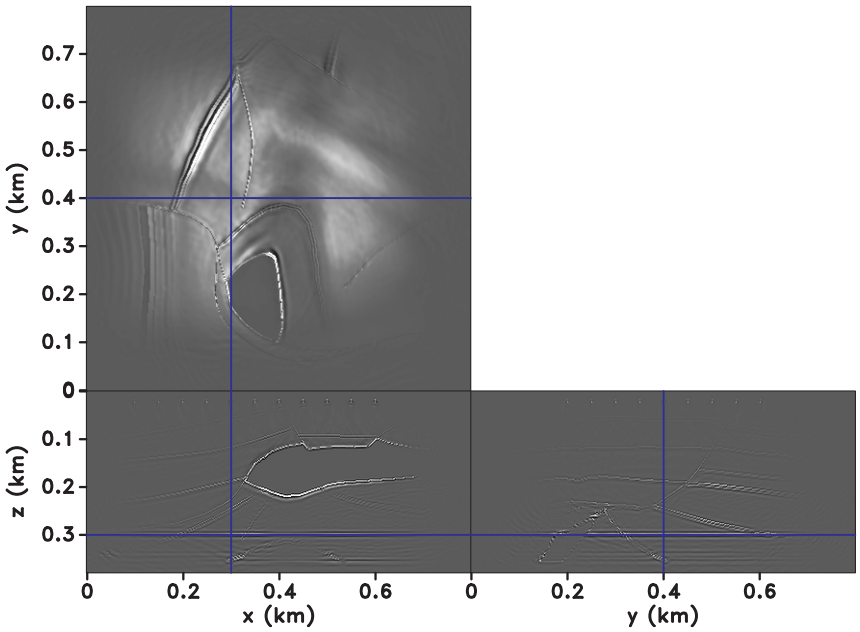
Yan, R., and X.-B. Xie, 2012, An angle-domain imaging condition for elastic reverse time migration and its application to angle gather extraction: Geophysics, **77(5)**, S105–S115.

Yang, T., and P. Sava, 2015, Image-domain wavefield tomography with extended common-image-point gathers: Geophysical Prospecting, **63**, 1086–1096.

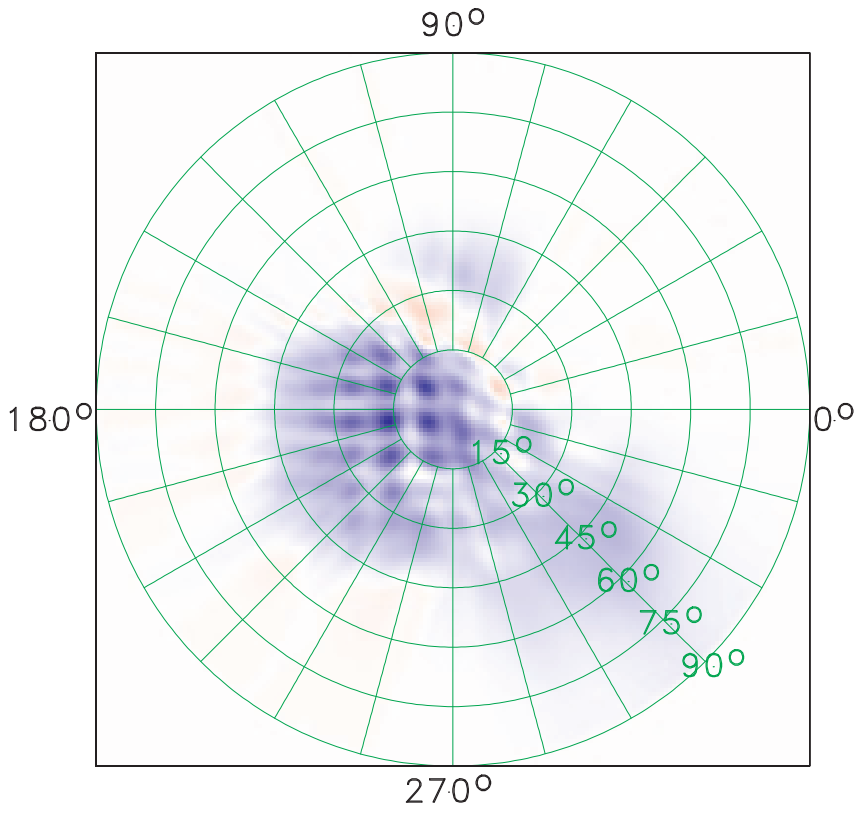
Yoon, K., and K. J. Marfurt, 2006, Reverse-time migration using the poynting vector: Exploration Geophysics, **37**, 102–107.

Yoon, K., K. J. Marfurt, and W. Starr, 2004, Challenges in reverse-time migration: Presented at the 2004 SEG Annual Meeting, Society of Exploration Geophysicists.

Zhang, Y., and J. Sun, 2008, Practical issues of reverse time migration-true-amplitude gathers, noise removal and harmonic-source encoding: Presented at the 70th EAGE Conference & Exhibition.

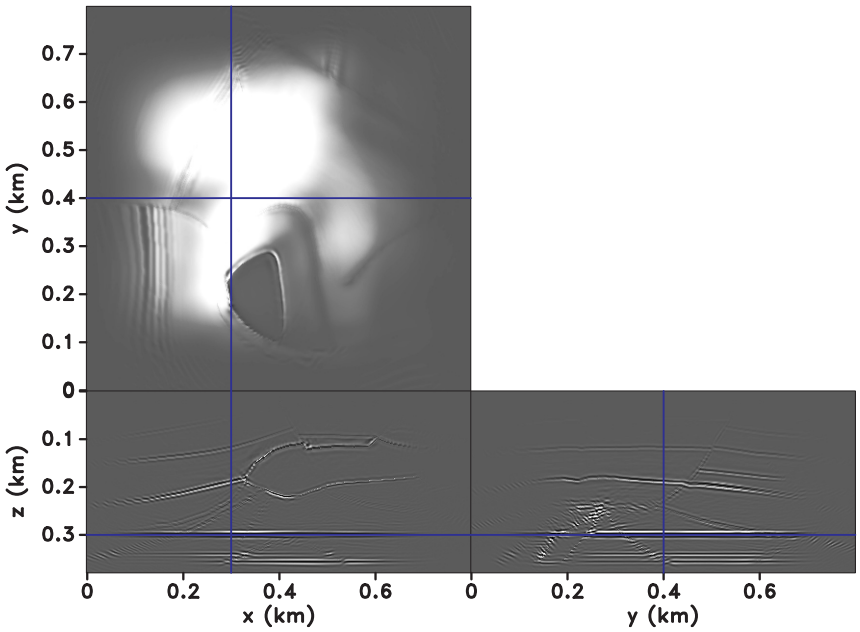


(a)

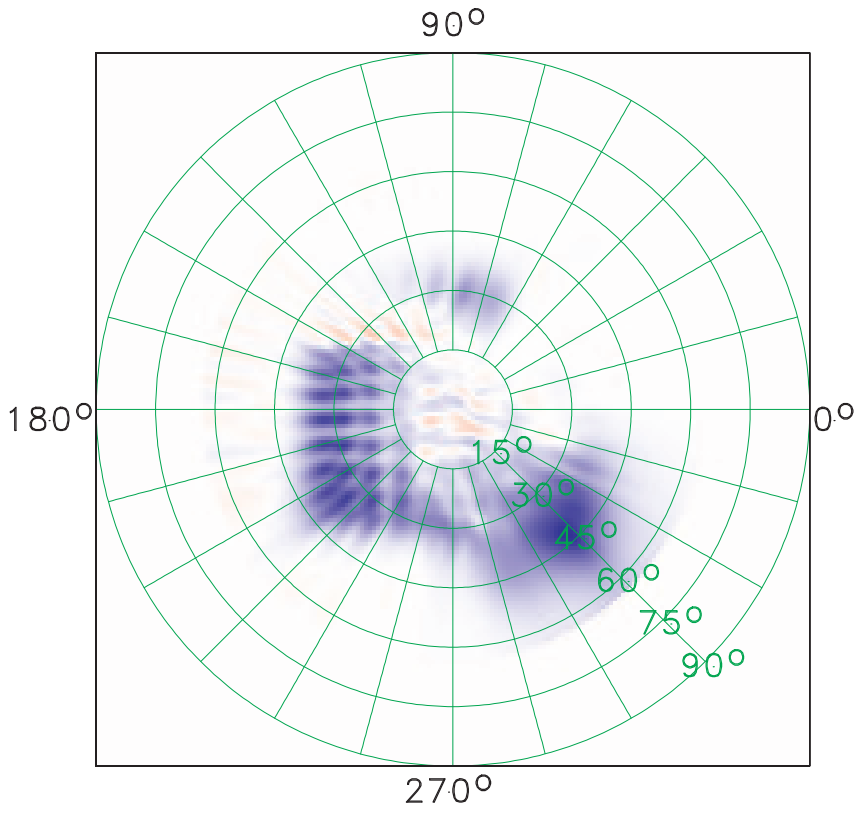


(b)

Figure 17. (a) PP image. (b) Angle and azimuth gather at coordinates $x = 0.3$ km, $y = 0.4$ km, $z = 0.3$ km, computed using the extended PP image.



(a)



(b)

Figure 18. (a) PS image. (b) Angle and azimuth gather at coordinates $x = 0.3$ km, $y = 0.4$ km, $z = 0.3$ km, computed using the extended PS image.